Available online at www.sciencedirect.com
SCIENCE DIRECT
Tectonophysics 420 (2006) 317–332
TECTONOPHYSICS
www.elsevier.com/locate/tecto

Effects of trench-zone scattering on receiver functions over a subduction zone: A 3-D finite-difference modelling study

Igor B. Morozov *, Haishan Zheng

Department of Geological Sciences, University of Saskatchewan, 14 Science Place, Saskatoon, Canada, SK S7N 5E2

Received 25 January 2005; received in revised form 10 October 2005; accepted 4 January 2006
Available online 11 April 2006

Abstract

As Morozov [Morozov, I. B. (2004). Crustal scattering and some artefacts in receiver function images. Bull. Seismol. Soc. Am., 94 (4), 1492–1499.] suggested, for a teleseismic array targeting subducting crust in a zone of active subduction, scattering from the strong horizontal velocity heterogeneity beneath the trench zone itself produces subhorizontally-propagating waves that should be observed as coherent dipping events in receiver functions (RF). Due to similar RF delay times and moveouts, these events could be difficult to distinguish from backscattered P- and S-wave modes. To further verify this suggestion, we performed a full-waveform, 3-D visco-elastic finite-difference modelling of teleseismic wave propagation within a simplified model of a subduction zone. The synthetics show strong scattering from the area beneath the trench, dominated by the mantle and crustal P-waves propagating at 6.2–8.1 km/s and slower. These scattered waves occupy the same time and moveout intervals as the backscattered converted modes, and also have similar amplitudes. Although their amplitude decay characters are different, the uncertainty in the knowledge of the velocity and density structure of the subduction zone could make distinguishing between these modes difficult. However, under minimal assumptions, recent observations of receiver function amplitudes decreasing away from the trench support the interpretation of (sub-) trench-zone scattering.

Although still limited in its representation of crustal heterogeneity, 3-D modelling suggests that scattering from near-Moho crustal structures plays a key role in the formation of teleseismic wavefields. Recognition of scattered noise in teleseismic records could help to constrain major crustal structures, particularly those with strong horizontal velocity contrasts at near-Moho depths, such as crustal sutures, subduction fault zones, and mountain roots. Matching of the observed arrivals with wavefield synthetics could help constrain the locations and parameters of such structures and also help substantiate the interpretations.

Keywords: Subduction zone; Converted waves; Receiver functions; Scattering; Modelling; Finite-difference; 3-D

1. Introduction

Teleseismic receiver functions (RF) are routinely used for imaging the Moho and upper mantle discontinuities, and they are viewed as the primary source of detailed information on the S-wave velocity contrasts within the upper mantle (e.g., Shearer, 1991; Bostock, 1998; Dueker and Sheehan, 1998; Shen et al., 1998; Sheehan et al., 2000; Bostock, 2003). RFs are highly useful for the imaging of strong subhorizontal velocity contrasts within the upper mantle, such as the Moho and (at lower frequencies) the transition zone discontinuities

* Corresponding author. Tel.: +1 306 966 2761; fax: +1 306 966 8593.
E-mail address: igor.morozov@usask.ca (I.B. Morozov).

0040-1951/$ - see front matter © 2006 Elsevier B.V. All rights reserved.
doi:10.1016/j.tecto.2006.01.016

(Chevrot et al., 1999). In the recent years, much effort was concentrated on higher-resolution imaging of the ~ 200-km depth interval below the Moho (Gurrola and Minster, 2000; Rondenay et al., 2001). Spectacular successes of array RF imaging were reported, particularly in continental subduction zone settings (Rondenay et al., 2001). However, opening of these imaging depth and dip intervals came at the cost of entering an environment of source-induced noise caused by the increased frequency and proximity to regions of strong crustal heterogeneity. The importance of these factors and their effects on the resulting images still have not been sufficiently studied.

As Morozov (2004) recently suggested, RF interpretations of the uppermost mantle may be sensitive to contamination of the coda by receiver-end crustal scattering. Teleseismic arrays typically target the deeper mantle structures and are often deployed with little regard for major crustal heterogeneities such as sedimentary basins or even plate boundaries. Because of a limited number of broadband instruments available, teleseismic experiments often use linear arrays deployed obliquely to the crustal structures (Fig. 1). In such recording environments, broadside noise caused by the primary arrivals scattered from such structures could be difficult to distinguish from the signals from depth. In controlled-source recording, such acquisition style is typically avoided, which unfortunately could be nearly impossible to do in teleseismic studies.

The increasing sophistication of multichannel RF imaging techniques also requires understanding of the potential artefacts introduced by the (predominantly crustal) broadside-scattered noise. Amplitude-based inversion methods extrapolated from reflection seismic imaging, such as the Generalized Radon Transform, allow inversion for multiple parameters of the mantle (V_P and V_S velocity and density perturbations; Bostock et al., 2001); however, these approaches also require complex model parameterizations and consequently increased sensitivity to the noise. In many cases, the imaging (e.g., depth migration) process serves as the primary instrument for noise suppression, which may not be adequate with sparse or aliased sampling, and particularly in the presence of coherent noise. Importantly, modern RF imaging approaches are based on prestack depth migration and use higher converted modes, such as backscattered S-waves (Bostock et al., 2001). These waves arrive at later times and may be buried in the background of crustal-scattered Pg, Sg, Pn, and Sn waves (Morozov, 2004). When migrated, these scattered arrivals lead to images similar to the dipping mantle structures of interest.

It is known that at frequencies above ~ 0.5 Hz, crustal scattering becomes predominant (e.g., Bannister et al., 1990; Gupta et al., 1990; Wagner and Langston, 1992; Clouser and Langston, 1995; Abers, 1998; Revenaugh, 2000). This frequency is close to the high-frequency end of RF imaging (Park and Levin, 2000), and it is also unclear how low should the frequency be in order for RF migrated images to be safe from corruption with the coherent noise. As a crude estimate, significant scattering could be expected from crustal heterogeneities of the size comparable to the wavelength. Major topographic features of ~ 10 km are not uncommon (Fig. 1), suggesting that coherent scattered waves could be observed at 0.2–0.5 Hz. More detailed estimates utilizing the details of the crustal structures surrounding the teleseismic arrays could be obtained by finite-difference modelling.

Active continental margins represent one of the best targets for such a modelling study. Some of these areas have been studied extensively and are characterized by generally well-understood subduction geometries as well by the largest crustal-scale velocity heterogeneities within and beneath the trench areas. Such linear heterogeneities could lead to pronounced inland-directed scattering that could be relatively easy to understand. The importance of starting from an example of a subduction zone is also emphasized by the fact that whenever a subducted crustal structure is recognized from its RF signature within the upper mantle, the hinge of that structure would also be likely to produce strong scattering with similar wavefield characteristics. Thus, on this example, we could also learn to differentiate the broadside-scattered noise from the arrivals from within the mantle.

Morozov (2004) attempted the first simplified modelling of teleseismic recording in a subduction zone, in geometry broadly similar to that of the 1993 PASSCAL experiment in Cascadia (CASC93; Nabelek et al., 1993; Trehu et al., 1994). To date, the unusually dense and linear CASC93 array represents a classical deployment targeting the subducting oceanic lithosphere. It was studied by a number of authors using different techniques, resulting in a number of spectacular images of the Juan de Fuca plate subducting beneath North America (Li, 1996; Rondenay et al., 2001; Bostock, 2002), and inspiring a number of other experiments (e.g., Meyers et al., 1999).

From his modelling of the scattering noise, Morozov (2004) found that the resulting synthetics exhibited strong similarities to RF events observed in similar experiments. The scattered noise contained similar frequencies, occupied the same space–time and moveout intervals as converted waves from the subducting

oceanic crust. From Born-approximation amplitude estimates, the noise was expected to be stronger or comparable to the converted wave amplitudes to ~ 400-km distances from the trench. Pre-stack depth migration of the scattered-noise records (particularly using assumptions of backscattered converted modes) resulted in spurious landward-dipping structures that could be confused with the subducting lithosphere. As an overall conclusion, this modelling suggested that interpretations of such images could become unreliable if broadside scattering noise was not properly isolated.

In this paper, we extend the modelling by Morozov (2004) to a full 3-D finite-difference simulation. Three-dimensional finite-difference modelling is often regarded as a realistic modelling method for arbitrarily complex models, and thus we expect that the resulting synthetic

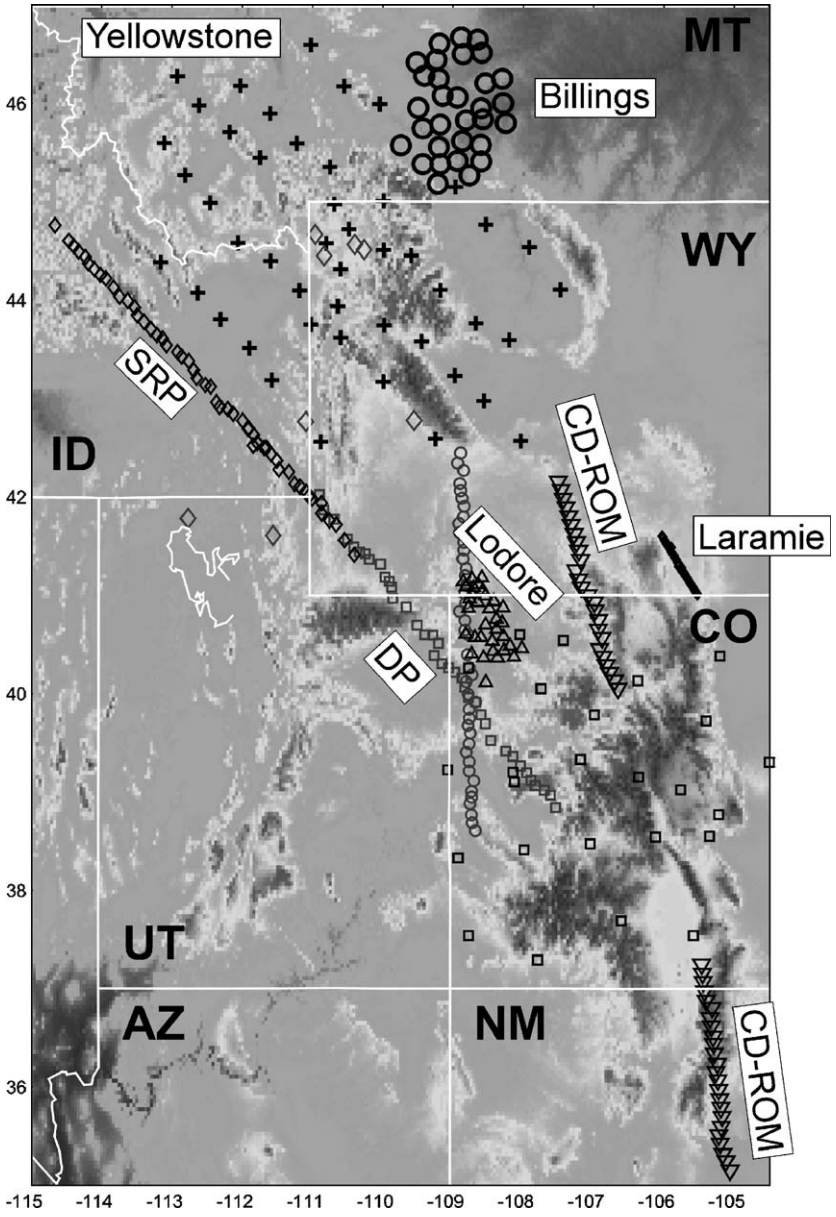

Fig. 1. Location map of seven recent IRIS PASSCAL teleseismic experiments in the Rocky Mountains, superimposed on the surface topography (figure courtesy of K. Dueker; modified). Note that the arrays are oriented based on the expected positions of the targeted mantle structures and on the predominantly NW–SE source back azimuths; however, these directions are also oblique or subparallel to major linear crustal structures, as suggested by the high topography. Together with the associated crustal heterogeneity, these structures could lead to image contamination by scattered noise. Abbreviations indicate: SRP — the Snake River Plain experiment, DP — Deep Probe, CD-ROM — Continental Dynamics of the Rocky Mountains.

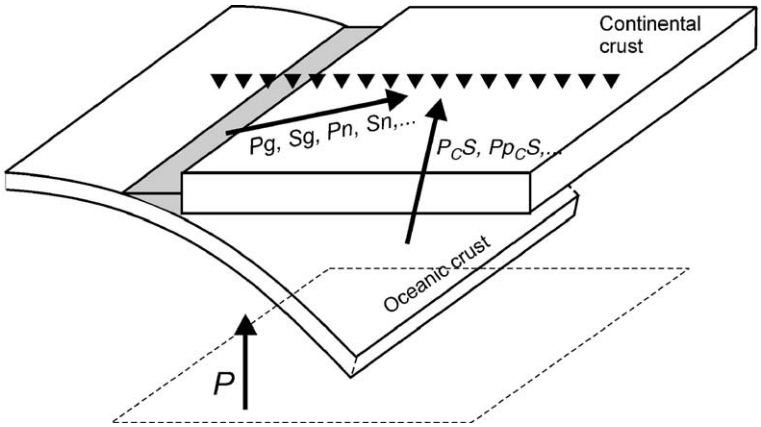

Fig. 2. Simplified model of trench-zone scattering (a similar model was considered by Morozov, 2004). Taking advantage of numerical modelling, we extend the teleseismic array (triangles) across the accretionary wedge (shaded grey) and use denser station spacing then practically possible at present (Fig. 3).

records would have reliable amplitude characteristics, thereby removing the heuristic convolutional model and Born approximation in the approach by Morozov (2004). In order to keep the model simple and comparable to the previous study, we retain the simplified geometry of the subducting oceanic crust and of the area of horizontal heterogeneity near the hinge of the subducting plate, broadly referred to as the "trench zone" in the following discussion (Fig. 2). The resulting synthetics confirm the general predictions of the previous study (Morozov, 2004), support its cautionary conclusions, and also provide a better insight into the complexity of trench-zone scattering. In addition, we investigate the possibilities and methods for separation of the converted waves from the trench-zone scattering, and also briefly investigate the effects of along-strike variations of the coastline.

2. 3-D modelling of a teleseismic array recording over a subduction zone

Schematically, the simulated model is shown in Fig. 2. A plane P-wave was incident from below onto a continental margin, and our objective was to compare the characteristics of the modes converted on the subducting oceanic lithosphere (P_DS, Pp_DS, Ps_DS) to those of Rg, Pg, Sg/Lg, Pn, Sn, and other phases generated in the trench area and propagating subhorizontally. Here, the converted wave nomenclature from Bostock (1998), where P, and S

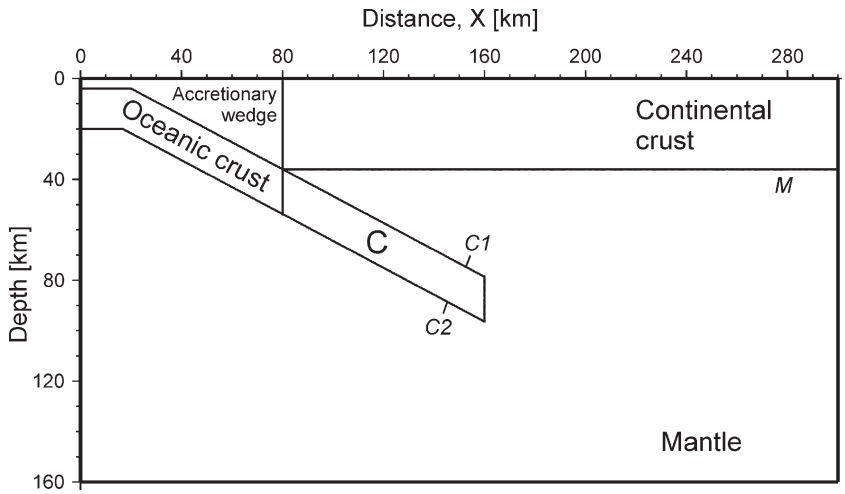

Fig. 3. Cross-section of the 3-D finite-difference model. 749 recording stations are spaced at 0.4 km apart along the top of the model. The segment of the subducting oceanic crustal slab labelled C is not included in the second simulation. Its upper and lower boundaries are labelled C1 and C2, respectively, and M indicates the continental Moho; this notation is also used in Fig. 4.

stands for upward-propagating waves, p and s for downgoing waves reflected from the free surface, and D denotes the converting velocity discontinuity. In our first simulation, the model was translationally-invariant along strike of the trench, and therefore the results should be comparable to those of 2-D modelling (however, note that only 3-D modelling correctly reproduces the geometrical divergence in all modes). The wavefield was recorded by a dense station array crossing the trench and extending onto the sea bottom. The details of the model are shown in Fig. 3. As an aid to event identification in the synthetic wavefield, we computed an approximate travel-time diagram by using ray kinematics (Fig. 4).

The model consisted of several blocks: continental and oceanic crust, subducting crust, and accretionary wedge overlying a mantle block. In each of the blocks, P- and S-wave velocities were gradually increasing downward in order to represent the average pressure-related trends (Table 1). In order to simplify the interpretation, no additional velocity discontinuities were introduced within the uppermost mantle or within the crust. Note that in order to provide only a conservative estimate of scattering, the velocities within the accretionary wedge were chosen comparatively high, $V_P = 6.0$ km/s (Table 1). Grid spacing was equal to 400 m, resulting in the total grid size of $750 \times 900 \times 200$ nodes. This grid was subdivided into $5 \times 6 \times 2$ processing sub-grids that were modelled concurrently in different processes. The wavefield was updated in 3000 time increments, with snapshots taken periodically, and the resulting surface velocities recorded at 749 locations along the entire upper axis of the model (Fig. 3).

Table 1
Model parameters (Fig. 3)

#	Block		V_P, km/s	V_S, km/s	Density, g/cm^3	Q_P	Q_S
1	Mantle		8.1	4.6	3.4	750	500
2	Continental crust	top	6.2	3.6	2.7	1000	1000
		bottom	7.0	4.05	3.0	2000	1500
3	Oceanic crust		7.0	4.05	3.0	2000	1500
4	Accretionary wedge		6.0	3.45	2.55	800	500
5	Subducted crust		7.0	4.05	3.0	2000	1500

Attenuation parameters are given at 0.5 Hz (centre frequency of the source), and one relaxation mechanism was used to simulate the frequency-dependence of Q (Bohlen, 2002).

Modelling was performed using a modified MPI (Message Passing Interface) parallel visco-elastic finite-difference program by Bohlen (2002). The typical run times for the simulations shown below were 10–12 h on our Beowulf cluster system using 33 dual 1.6 GHz Opteron processors. Exponential

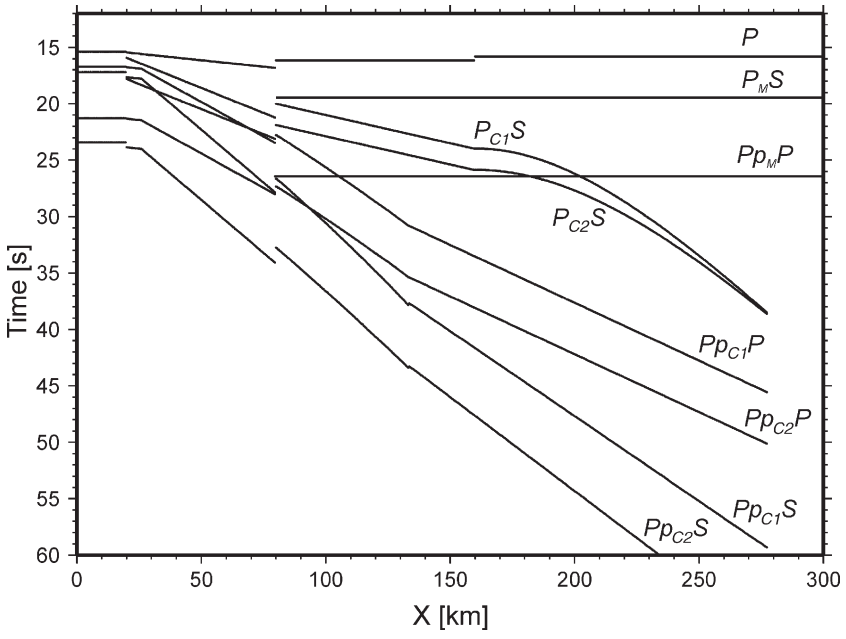

Fig. 4. Travel-time diagram showing the main converted phases within the model. Seismic phases scattered on the trench zone are not considered for clarity. Phases are labelled using uppercase P and S for the upcoming waves, lowercase p — for downgoing P-wave reflections from the surface, and interface designators (C1, C2, or M; Fig. 3) — for the reflecting or converting interfaces (Bostock, 1998). Note the Moho P_MS conversion and Pp_MP multiple, and also the forward- and backscattered converted modes from the top and bottom of the subducting oceanic crust. Also note the hyperbolic diffraction tails of two Pp_CS conversions caused by truncation of the subducted slab at km 160 in our model (Fig. 3).

damping was used to suppress reflections from the sides and bottom of the model. This damping was still unable to remove spurious scattering caused by the coupling of the primary wave with the side edges of the model, and periodic boundary conditions were applied to eliminate this coupling. Unfortunately, this could be achieved for only vertically-propagating P-wave and at the cost of obtaining some wrap-around artefacts which, however, did not prevent interpretation. Free-surface (zero stress) boundary condition was applied at the top of the model. No water layer was considered in this simulation because its effect was not deemed critical yet its low velocity would lead to a substantial increase of the computational load.

A 0.5-Hz Ricker wavelet was used as the P-wave source function. The dominant signal frequency was determined from the requirement of having the minimum of 8 grid points per the shortest *S*-wave length, leading to

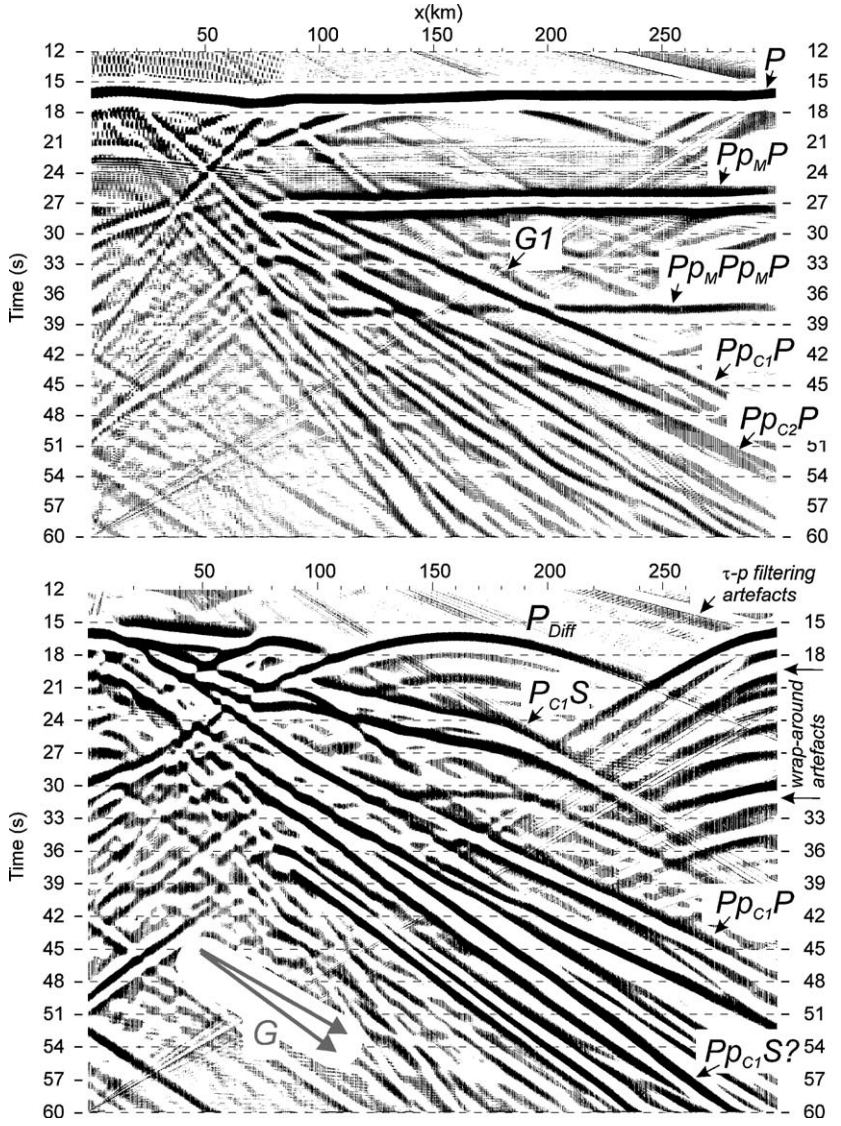

Fig. 5. Vertical (top) and horizontal component (bottom) simulated velocity response of the model (Fig. 3) to a single plane P-wave incident directly from below. The main phases are labelled (compare to Fig. 4). Note the strong band of trench-scattered energy (most prominent with velocities of ~ 8.1, 6.2 (moveouts marked with arrows labelled G), and ~ 2.9 km/s. These guided waves occupy the same time–dip interval as the Pp_CS modes and significantly interfere with Pp_CP. Also note the strong downward-bending diffraction from the lower edge of the subducting slab (labelled P_{Diff}). The upward-dipping events in the lower-right part of the section are wrap-around effects caused by the use of periodic boundary condition during modelling. These wrap-around artefacts were reduced by τ–p filtering; however, applications of the τ–p filter also resulted in low-amplitude down-dipping events visible in the upper part of the section.

less than 2% of numerical dispersion (Robertsson et al., 1994; Bohlen, 2002). The plane wave was generated by introducing an "exploding" pressure surface at the depth of 150 km followed by muting out the downward-propagating wave after 5 s of time stepping. Because of the limitations of the existing code, only vertically-propagating P-waves could be simulated without significant edge artefacts. This limitation should be removed in the future. However, as indicated by the wave kinematics analysed by Morozov (2004), variations in the ray parameter within its typical for RF imaging range of $p \approx 0.06$ s/km do not significantly affect the mutual positions of the trench-zone noise in respect to the mode conversions, and therefore the simulations at $p = 0$ s/km still are sufficiently representative.

The resulting synthetic wavefield generated by a single plane wave from below is shown in Fig. 5 With the help of Fig. 4, most modes converted on the subducted oceanic crust can be identified (labelled in Fig. 5). However, only the earliest of these modes, P_CS, arrives within the interval that is relatively free from multiples and trench-zone scattering. Backscattered modes (Pp_CP and particularly Pp_CS, and others) lie within the region contaminated with waves scattered from the trench zone. Most significant of these scattered waves propagate at the uppermost-mantle and crustal P-

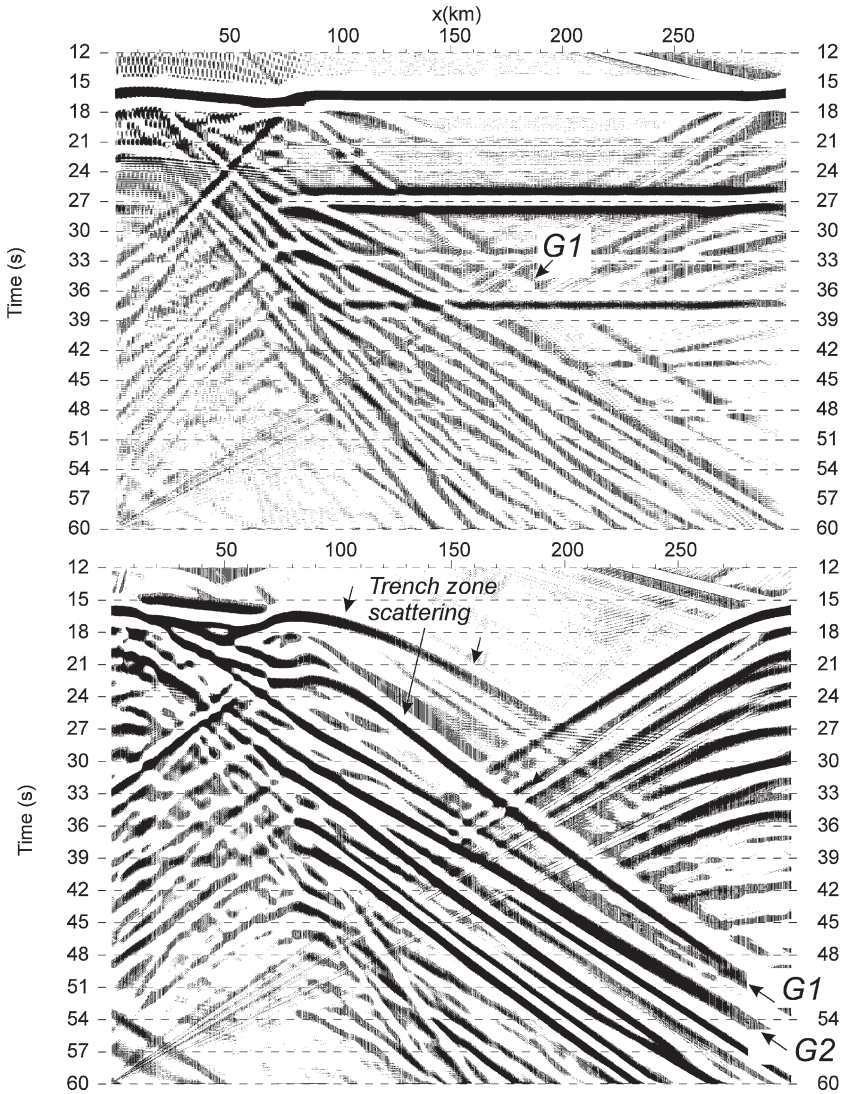

Fig. 6. Same as Fig. 5 but modelled without the subducted portion of the slab (labelled C in Fig. 3). Note that the wavefield within the Pp_CP and Pp_CS time–moveout intervals (defined in Fig. 4) is still complex and close to that in Fig. 5. Also note the difference in the scattered wavefields in two directions from the trench area, which should be caused by the shape of the scattering velocity–density contrasts at crustal and near-Moho depths.

wave velocities (~ 8.1 and 6.2 km/s; Fig. 5), although some contribution from the surface waves (with velocities of 2.9 km/s) is also present. These observations support the suggestion by Morozov (2004) that with bottom-side excitation, scattered Pn and Sn waves should carry significant energy that could overwhelm the backscattered converted wave responses.

In order to separate the effects of the trench zone from those of the subducted oceanic crust, we simulated the wavefield in a model without the sub-crustal oceanic block (Fig. 6). The resulting synthetics are different yet quite similar to those in Fig. 5. within the Pp_CP and Pp_CS time–moveout windows. Clearly, migration of these synthetics assuming a backscattered (particularly Pp_CS) converted mode kinematics could lead to an erroneous image of a dipping structure similar to the subducted crustal block in our model (Fig. 3).

Subtraction of the section in Fig. 6 from that in Fig. 5 emphasizes the response of the subducted crustal block alone (Fig. 7). The converted waves, including the backscattered modes Pp_CP and Pp_CS, stand out more clearly in this image, and the trench-zone scattering noise

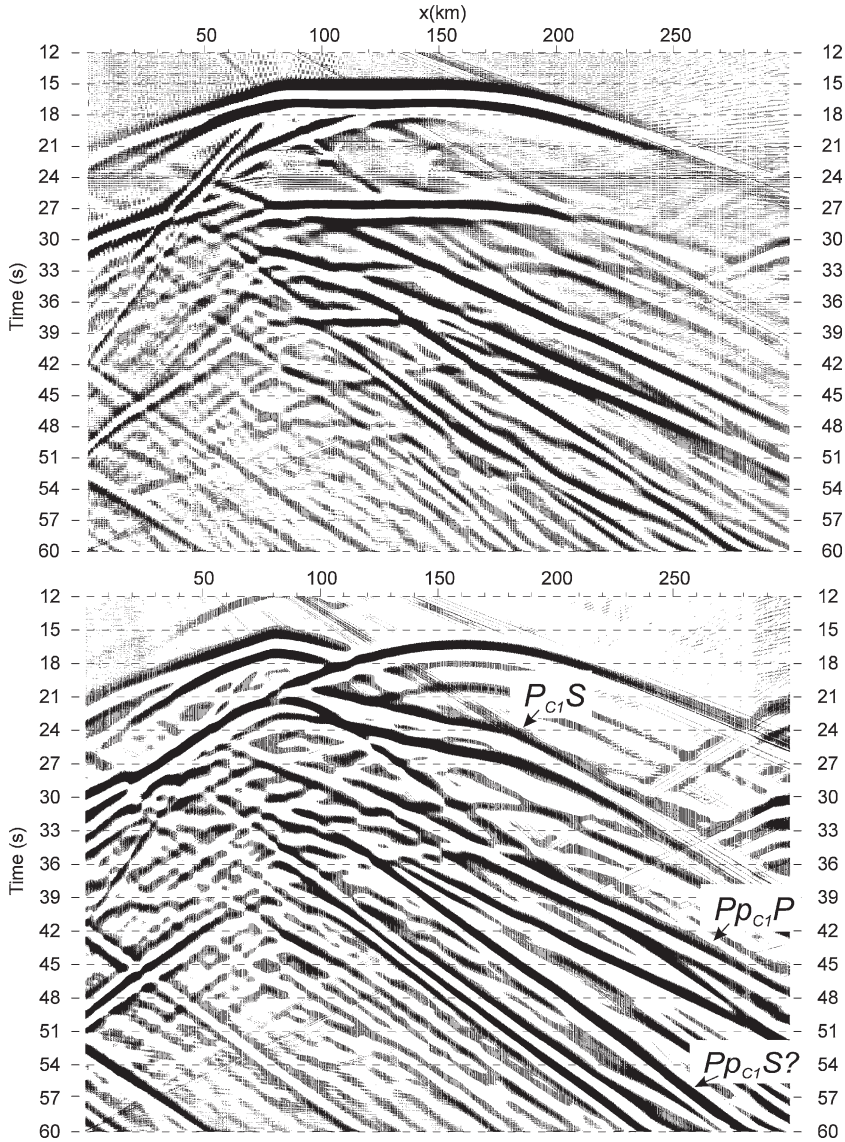

Fig. 7. Result of subtraction of the between the wavefields modelled with and without the subducted portion of the slab (Figs. 5 and 6). This display emphasizes the response from the subducted oceanic crust, including diffractions from both of its ends and multiples and conversions from the free surface and Moho. Note that as the timing of the waves propagating through the subducted slab was also disturbed by its removal, some additional spurious events appeared in this image.

is reduced. However, a complex background of scattered arrivals is still present, caused by diffractions on the edges of the block and by multiple reflections and conversions from the free surface and the Moho. In addition, removal of the subducted crustal bock also changes the timing of the primary P-wave and of the later modes propagating through its volume, and therefore the resulting differential wavefield still does not match the ray diagram (Fig. 4) completely.

Finally, Fig. 8 shows the results of another modelling in which the low velocities within the sedimentary accretionary were removed, and the crustal velocity profiles at all locations were set equal to that of the continental crustal block. This simplified model thus retains the shape of the crust–mantle contact while disregarding the effects of crustal velocity heterogeneity. Note that although strong trench-zone scattering is still present, the resulting wavefield is significantly simpler, with mode content closer to the accepted paradigm of RF interpretation. Only in this case it becomes possible to identify the backscattered S-wave (Pp_CS) mode with reasonable confidence (Fig. 8). However, although also being a simplification, Fig. 5 utilizes a far more realistic crustal model of a subduction zone, and thus the velocity/density

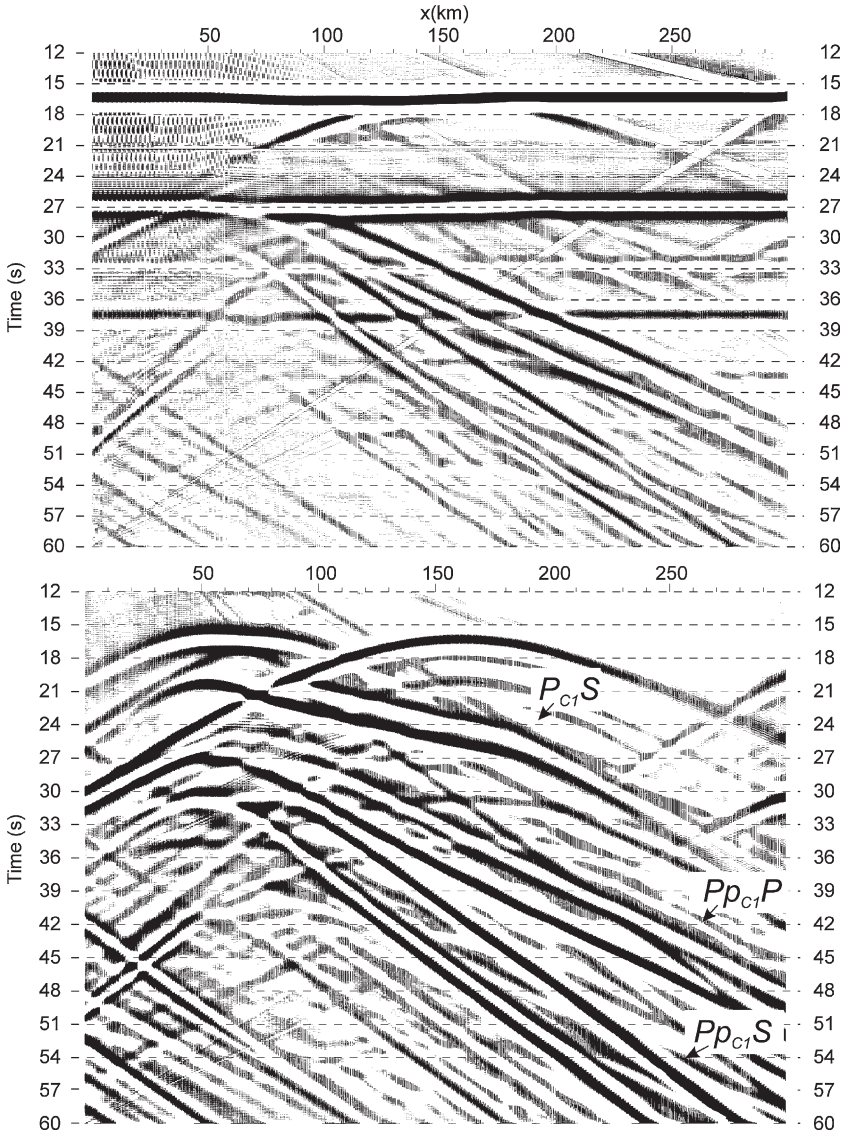

Fig. 8. Modelling results for the same structure (Fig. 3) but with crustal velocities only depth-dependent and following the depth–velocity profile of the continental crustal block. Compare to Fig. 5 and note that removal of the horizontal velocity contrasts in the vicinity of the accretionary wedge leads to significant simplification of the resulting wavefield. Only in this case we can identify the backscattered Pp_CS mode with some confidence.

heterogeneity caused by the accretionary wedge effects should definitely be considered in the interpretation.

3. Discussion

Numerical modelling could provide useful guidance for interpreting teleseismic data, particularly at higher frequencies at which the Earth's structure significantly deviates from the pressure-dominated 1-D velocity–density distribution. Modelling offers several unique advantages, of which the first is the controlled-source signal of a simple shape. The resulting sections (Figs. 5, 6 and 8) can therefore be viewed as source-normalized three-component receiver functions (Langston and Hammer, 2001). The second advantage offered by synthetic modelling is the ability to analyse wavefield snapshots, such as those in Fig. 9 showing the development of the seismic waves scattered on the trench zone and on the subducted crustal block within our model. As expected, even for this simple crustal structure, the wavefield is

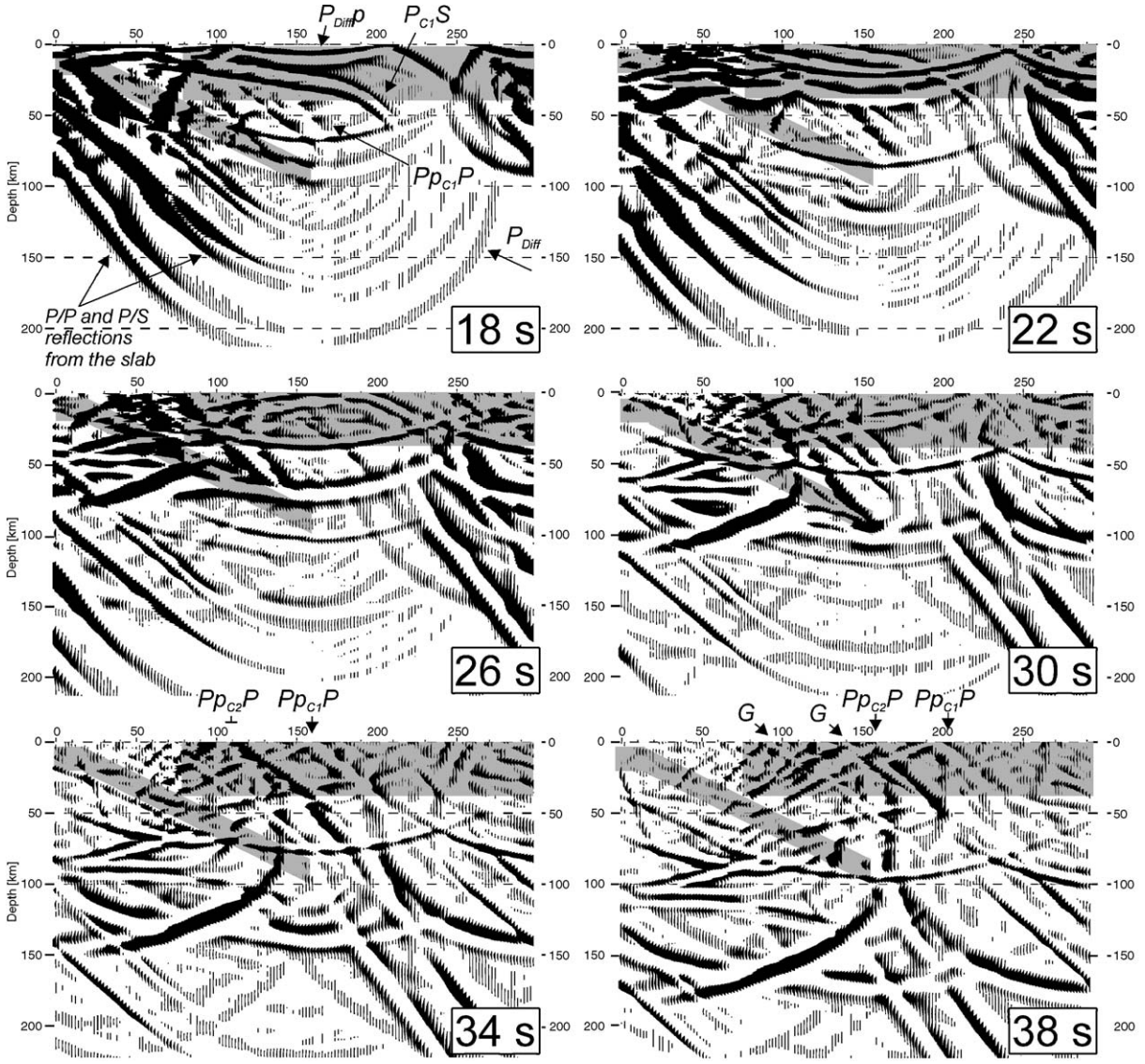

Fig. 9. Snapshots of the horizontal component of the wavefield in the model of Fig. 3 at selected times starting at ~ 2 s after the primary P-wave onset (labelled). Model blocks (Fig. 3) are shown in grey backdrop. The P_CS mode conversion and the backscattered Pp_CP reflection are indicated. Note the crustal-guided waves generated in the trench area, labelled G (as in Fig. 5). These waves stay near the Pp_CP and later phases throughout the entire propagation process. Note the strong downside reflections and conversions from the subducted crustal block propagating down and to the left. Because of the periodic boundary condition, these phases also appear in the upper-right corner of the model and propagate to the left.

quite complex and is not dominated by waves converted on the subducted crust. Dip angles of the wavefronts as they are approaching the surface are indicative of the apparent velocities of the corresponding phases. Note how the trench-scattered waves (labelled G) sweep along the receiver array at both the times and apparent velocities close to the backscattered Pp_CP reflection and Pp_CS mode conversion from the slab.

In regards to the potential ways for separating converted arrivals from the subducted slab from the subhorizontally-propagating scattered modes, two groups of methods can be considered: based on their time–moveout characteristics or amplitude dependencies. Even in the case of dense (unaliased) recording, moveout (f–k or τ–p) filtering cannot achieve such separation in a record from a single earthquake. For multiple sources, moveouts of the trench-zone scattered events would remain constant while those of converted waves would vary, giving a potential criterion for separation. However, implementation of this analysis would still require multiple closely spaced sources with confidently correlated coherent arrivals, which could present a problem in practice. A potentially more realistic, single-event mode separation criterion could be based on the dependencies of their amplitudes on the distance from the trench (Morozov, 2004). In an attenuation-free case, scattered waves would exhibit a near-cylindrical geometrical spreading while the converted modes would be of approximately constant amplitudes. With attenuation taken into account, these amplitudes would additionally decrease landward with the different trends remaining.

In our synthetics (Figs. 5, 6 and 8), the amplitudes show distinctly different decay patterns with increasing landward distances (Fig. 10). As expected for this model with vertical velocity gradients and finite attenuation (Table 1), scattered waves decrease in their amplitudes faster than prescribed by cylindrical geometrical spreading of $1\sqrt{r}$, where r is the distance from the trench. By contrast, backscattered waves reflected or converted on the surface of subducted crustal slab have generally constant amplitudes or even increase within the extents of the slab (Fig. 10). This difference in amplitude patterns could potentially

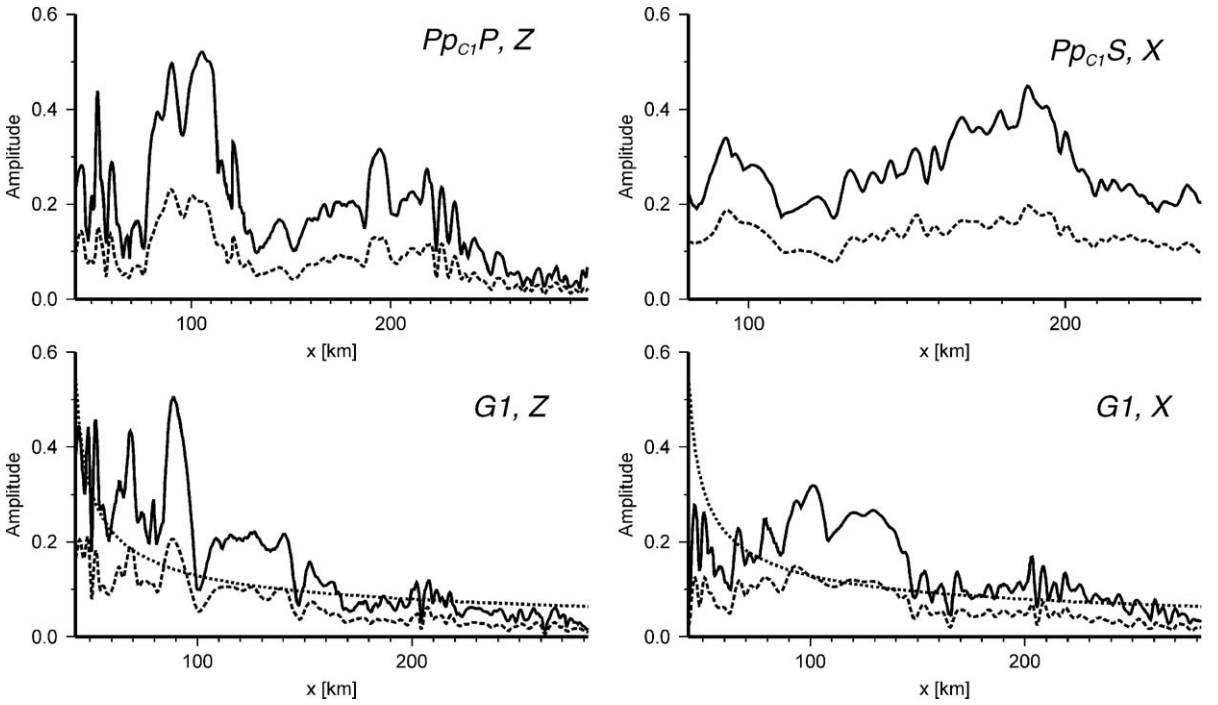

Fig. 10. Amplitude dependences of: (1) the backscattered Pp_CP reflection and Pp_CS mode conversion on the oceanic crustal slab (Fig. 5) and (2) vertical (Z) and horizontal (X) components of a trench-scattered mode labelled G1 in Figs. 5 and 6. Identical amplitude scaling is used in all four plots. In all plots, the upper (solid) lines show the peak absolute value amplitudes of the corresponding phases, and dashed lines give their RMS amplitudes. In G1 plots (bottom), thin dotted lines indicate the reference $1/\sqrt{r}$ dependence, where r is an approximate distance from the trench area. Note that unlike the slab-converted modes, amplitudes of the trench-scattered waves decrease along the profile. However, observation of these trends is complicated by amplitude fluctuations caused by multiple interfering arrivals. Also note that the scattered-wave amplitudes (G1) are underestimated due to the use of very high-velocity sediments (Table 1).

be used to distinguish between the interfering backscattered and trench-scattered phases (Fig. 5). Tentatively, CASC93 receiver function sections (Fig. 3 in Rondenay et al., 2001) suggest a consistent drop in the observed amplitudes with distance, supporting the trench-zone scattering model. However, an unambiguous distinction in this and most likely also other cases could be difficult because of several factors. First, if the hypothesis of dehydration and eclogitization of the subducting crust is invoked (Hacker, 1996; Rondenay et al., 2001), seismic response of the slab could be reduced with depth in a complex manner, thereby somewhat devaluating the proposed criterion. Interference of multiple modes modulates both of these amplitude–distance dependencies creating localized amplitude highs and lows (Fig. 10) that are sensitive to the crustal and uppermost-mantle structure. With spatial sampling sparser than in our numerical experiment, varying site effects could also complicate amplitude analysis of real field data. However, with dense deployments, true-amplitude waveform analysis and detailed numerical modelling could in principle help to distinguish backscattered mode conversions from broadside-scattered waves.

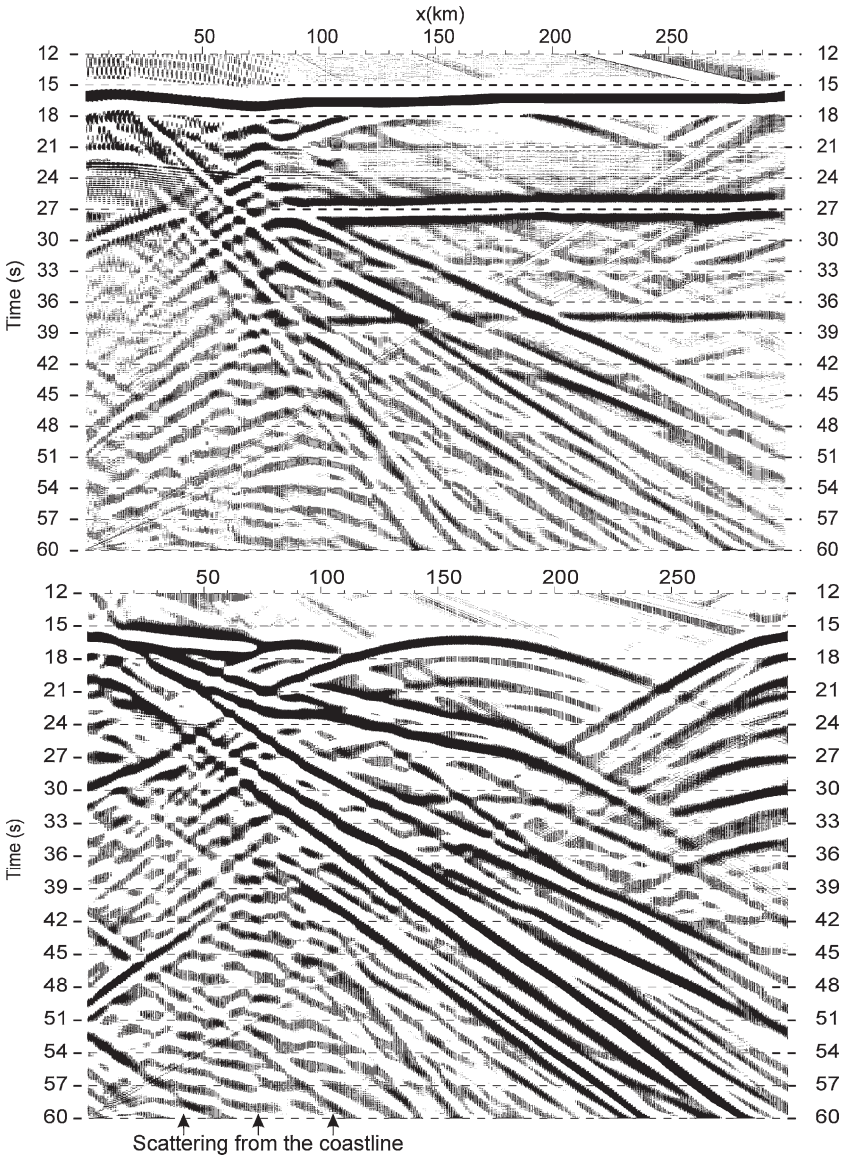

Fig. 11. Illustration of the effects of a sinusoidal along-strike variation of the continental coastline. Compare to Fig. 5. Note the characteristic scattering pattern similar to one often observed in crustal reflection and RF records.

Topographic scattering is a major issue that deserves a special study. As a first illustration of its effects, we consider the influence of an along-strike variability of the trench zone (Fig. 11). For this simulation, we introduced a ±25-km sinusoidal variation of the position of the coast in the original model (Figs. 2 and 3), with a wavelength of 40 km along strike. The shapes and thicknesses of the oceanic crustal blocks, and all velocities and densities were unchanged, and thus the resulting scattering should be concentrated within the part of the model beneath the trench zone. As expected, the resulting synthetics (Fig. 11) exhibit the same general pattern as in Fig. 5. However, in the cone of relative quiescence from the trench-scattered noise (~ 30–60 s in the area of the trench), an additional reverberatory and subhorizontal noise pattern is also seen (labelled in Fig. 11). Because the model includes no other in-line scatterers, these subhorizontal arrivals should be due to the scattered waves predominantly propagating along the coast (i.e., broadside to the line of our cross-section). Additional topography east of km 50 (e.g., the volcanic arc associated with the subduction) would clearly extend this zone of scattered noise eastward. Also note that similar noise patterns are common in deep crustal reflection records, where they should also be due to broadside near-surface scattering.

Of all the modes converted or refracted on the subducted crust (Fig. 4.), only the top- and bottom-side forward P_CS conversions beyond the distances of ~ 60 km from the trench are free from contamination by the trench-zone scattering in our simulation (Fig. 5). This suggests that observations of P_CS responses could generally be more reliable indicators of the true mantle structures. However, a word of caution is due even in this case: the model described above is still overly simplified to predict a realistic response in this zone of relative quiescence. This range of distances from the trench is nearly always characterized by series of volcanic arcs with high surface topography and (presumably) pronounced Moho relief, such as the Coast and Cascade Ranges in the case of CASC93 array. These structures should produce complex noise background with similar pronounced appearance of dipping and subhorizontal events that still need to be examined by detailed modelling and comparison to the available data.

Imaging algorithms disregarding the side-scattered modes, such as even 3-D, true-amplitude converted mode migration could hardly be relied upon for suppression of the scattered arrivals. In realistic imaging situations, event-filtering capabilities of RF migration (and also inversion, or stacking) are limited by several factors, and particularly by 1) the conflicting assumptions of mode content (P_CS, Pp_CS, Ps_CS, etc.), which are expected to be separated by the migration process itself, 2) limited extents (apertures) of the arrays not crossing or even approaching the zone of scattering, and 3) the limited number of sources and narrow range of their ray parameters. In addition, recovery of the true RF amplitudes, which could potentially be used for identification of the broadside-scattered modes, is difficult because of complex recording site effects and imperfect RF deconvolution.

Because of a limitation of the present modelling algorithm (strong edge artefacts when modelling plane waves at non-vertical incidence), we only consider a single vertically incident arrival here (Figs. 5 and 6), which is insufficient for migration. However, an insight

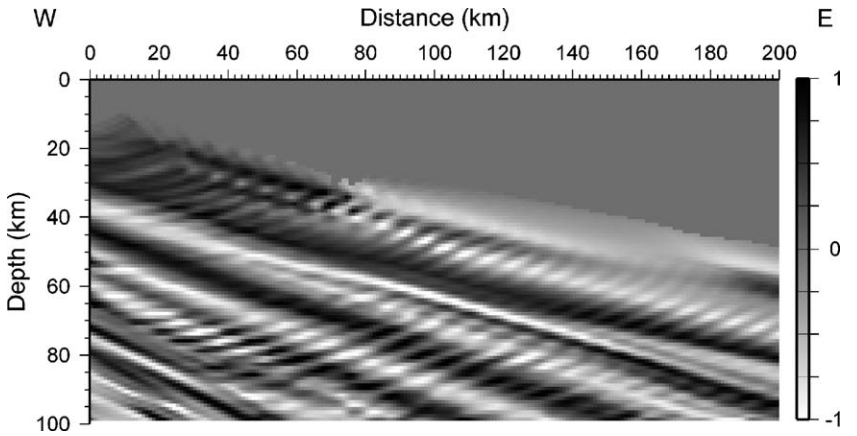

Fig. 12. Migration of trench-zone scattered wavefields (modelled without the subducted crustal block) assuming the Pp_CS mode kinematics (modified after Morozov, 2004). Migration was performed in 3-D (Morozov and Dueker, 2003b), with full account for the out of plane effects and using the CASC93 source distribution from Rondenay et al. (2001).

into the effects of effects of the trench-zone scattering on depth migration could be gleaned from the analysis by Morozov (2004). Even with significantly simpler scattering-zone response considered in this work, superimposition of the different sources intermixed the scattered-wave artefacts and lead to complex interference patterns showing nearly any dips steeper than ~ 10° (Fig. 12). Consequently, spurious dipping patterns should also dominate migrated images produced from full-waveform synthetics similar to those in Figs. 5 and 6. Note that compared to the more commonly used 2-D migration (e.g., Rondenay et al., 2001; Nowack et al., 2003), 3-D migration (used in Fig. 12) not only does not alleviate but is more likely to aggravate this problem, because it is far stronger under-constrained with the limited data. However, there hardly is any alternative to 3-D imaging with teleseismic data.

The broadside-scattered mode synthetics are dominated by the waves propagating at mantle and crustal compressional body wave velocities (8.1 and 6.2 km/s) and to a significantly smaller degree — by the surface waves (Fig. 6). The relatively low contribution of the surface and S-waves could be explained by two factors: 1) the excitation from below, as suggested by Morozov (2004), and 2) by the use of a simple transparent continental crustal model, with no surface or Moho topography and no crustal velocity heterogeneities. Also, the amplitudes scattered from the sedimentary wedge are likely to be underestimated by in our example by a factor of 2–3 due to the high velocities used for the sediments (Table 1). The example considered here is still an idealization designed to illustrate the key crustal effects on the wavefield without completely obliterating the converted modes. With a more realistic crustal heterogeneity included, significantly stronger P- to S-wave scattering could be expected from within the crust.

Apart from contributing unwanted artefacts into the converted wave images of the mantle, broadside crustal scattering could potentially be used to locate and constrain crustal and uppermost-mantle heterogeneities, particularly near the Moho level. Along with the accretionary trench zones discussed above, intracontinental targets of such kind could be crustal-scale fault zones projecting into the mantle and related to shallow and oblique lithospheric subduction (Bostock, 1998). Such zones were reported in Lithoprobe reflection studies (Cook et al., 1997). Teleseismic arrays deployed near such structures would be likely to detect scattering caused by the associated Moho relief, rugged topography, coastlines, sedimentary basins, and crustal faults (Abers, 1998; Revenaugh, 2000; Morozov, 2004).

Ideally, a way to evaluate and utilize the effects of broadside crustal scattering would be to deploy a teleseismic array across and on both sides of the scattering structure, as it is done in our model (Fig. 3). In the case discussed here (Fig. 2), subducting oceanic crust is expected only to the east of the trench while the scattered field would be recorded in both directions (Fig. 6). However, leaving aside the difficulties of broadband recording on the sea bottom, the synthetic modelling also shows that even with such a deployment, the scattered wavefield could be significantly different in the two directions (Fig. 6), and therefore the presence of backscattered modes (Pp_CP, Pp_CS, etc.) on its background could still be difficult to establish with confidence.

Finite-difference modelling could be most useful for planning teleseismic experiments, in a way it is routinely done in the seismic industry (e.g., Cooper, 2004). With the advent of cluster computing utilizing commodity hardware and free software, 3-D finite-difference visco-elastic modelling is becoming practical and affordable (Bohlen, 2002). Because teleseismic waveform modelling utilizes relatively low-frequency waves, only limited numbers of sources, and reasonable complexity of velocity models, 3-D finite-difference modelling could be performed relatively quickly and with resolution adequate for quantitative comparisons with the field data. Synthetic datasets could be used in order to test and calibrate the imaging methods, including the 3-D prestack depth migration (Morozov and Dueker, 2003b) and to estimate the projected image quality (Morozov and Dueker, 2003a), again, similar to the petroleum exploration industry (e.g., Long, 2004). Finally, for a teleseismic experiment, such modelling would likely take less than 1% of the time allotted for the field work.

4. Conclusions

With the use of cluster computer systems, teleseismic waveforms can be modelled using visco-elastic finite-difference approaches in three dimensions and at realistic degrees of resolution. In this study, we modelled the full-waveform wavefield scattered within a simplified model of a subduction zone, including the oceanic and continental plates, subducted oceanic crust, and an accretionary sedimentary wedge.

The resulting synthetics support the cautionary conclusions from the study by Morozov (2004). The wavefield shows strong scattering from the trench zone, dominated by the mantle and crustal P-waves propagating at 6.2–8.1 km/s. These scattered waves occupy the same time and moveout intervals as the backscattered

modes reflected or converted on the subducted oceanic crust. Given the complexity of the subduction zone and the range of possible assumptions about the properties of subducting crust (e.g., its dehydration), a distinction between the backscattered reflected or converted modes appears still difficult. At the same time, without making special assumptions such as slab dehydration, the observed receiver function amplitudes decreasing away from the trench strongly support the trench-scattered mode interpretation.

When migrated assuming backscattered converted wave kinematics, the broadside-scattered noise gives rise to imaging artefacts that may appear as dipping mantle structures. The noise patterns, and consequently the appearance of these structures change with the variations of the shape of the trench zone and of the source distribution. Forward-scattered PS mode conversions on the subducted slab are relatively noise-free; however, this still could be due to the oversimplification of the present model that does not include surface or Moho topography within the arc region.

Without an account for the receiver-end broadside crustal scattering, RF interpretations, including multi-channel, pre-stack, multi-modal depth imaging may be subject to a danger of misinterpretation. In particular, for linear structures dipping steeper than ~ 10° and particularly those constrained by backscattered-mode imaging, alternative interpretations of the RFs as resulting from scattered waves originating at the hinge of that structure should also be considered.

Finally, recognition of scattered noise in teleseismic records could be useful in locating major crustal structures, particularly those with strong horizontal velocity contrasts at near-Moho depths, such as crustal sutures, subduction fault zones, and mountain belt roots. Correlation of the observed arrivals with wavefield synthetics could help constrain the locations and parameters of such structures and also help substantiate the interpretations.

Acknowledgements

This research was supported in part by Canada NSERC Discovery Grant RGPIN261610-03 to I. Morozov. Thomas Bohlen provided the parallel visco-elastic finite-difference modelling code. We thank Dr. Bohlen, an anonymous reviewer, and Guest Editor David Eaton for their careful and constructive reviews of the original manuscript. One of the authors (I.M.) thanks Bob Nowack, Gary Pavlis, and Scott Smithson for their encouragement and numerous enlightening discussions.

References

Abers, G.A., 1998. Array measurements of phase used in receiver function calculations: importance of scattering. Bull. Seismol. Soc. Am. 88, 313–318.

Bannister, S.G., Husebye, E.S., Ruud, B.O., 1990. Teleseismic *P* coda analysed by three-component and array techniques: deterministic location of topographic *P*-to-*Rg* scattering near the NORESS array. Bull. Seismol. Soc. Am. 80, 1969–1986.

Bohlen, T., 2002. Parallel 3-D viscoelastic finite difference seismic modelling. Comput. Geosci. 28, 887–899.

Bostock, M.G., 1998. Mantle stratigraphy and evolution of the Slave province. J. Geophys. Res. 103, 21183–21200.

Bostock, M.G., 2002. Kirchhoff-approximate inversion of teleseismic wavefields. Geophys. J. Int. 149, 787–795.

Bostock, M.G., 2003. Linearized inverse scattering of teleseismic waves for anisotropic crust and mantle structure: 1. Theory. J. Geophys. Res. 108, 2258. doi:10.1029/2002JB001950.

Bostock, M.G., Rondenay, S., Shragge, L., 2001. Multi-parameter 2-D inversion of scattered teleseismic body waves — I. Theory for oblique incidence. J. Geophys. Res. 106, 30,771–30,782.

Chevrot, S., Vinnik, L., Mintagner, J.P., 1999. Global-scale analysis of the mantle Ps phases. J. Geophys. Res. 104, 20,203–20,219.

Clouser, R.H., Langston, C.A., 1995. Modelling observed P–Rg conversions from isolated topographic feature near the NORESS array. Bull. Seismol. Soc. Am. 85, 195–211.

Cook, F.A., Van der Velden, A.J., Hall, K.W., 1997. Upper mantle reflectors beneath the SNORCLE transect: images of the base of the lithosphere? In: Cook, F., Erdmer, P. (Eds.), Slave-Northern-Cordillera Lithospheric Evolution (SNORCLE) Transect and Cordilleran Tectonics Workshop Meeting. Lithoprobe Rep., vol. 56. Univ. of Calgary, Alberta, pp. 58–62.

Cooper, N., 2004. A world of reality — designing land 3D programs for signal, noise, and prestack migration, Part 1 of a 2-part tutorial. Lead. Edge 23 (10), 1007–1014.

Dueker, K.G., Sheehan, A.F., 1998. Mantle discontinuity structure beneath the Colorado Rocky Mountains and High Plains J. Geophys. Res. 103, 7153–7169.

Gupta, I.N., Lynnes, C.S., McElfresh, T.W., Wagner, R.A., 1990. F–K analysis of NORESS array and single-station data to identify sources of near-receiver and near source scattering. Bull. Seismol. Soc. Am. 80, 2227–2241.

Gurrola, H., Minster, J.B., 2000. Evidence for local variations in the depth to the 410-km discontinuity beneath Albuquerque, New Mexico. J. Geophys. Res. 105, 10,847–10,856.

Hacker, B.R., 1996. Eclogite formation and rheology, buoyancy, seismicity, and H_2O content of oceanic crust. in: Bebout, et al. (Ed.), Seduction from top to bottom. Geophys. Monogr. Ser., vol. 96. AGU, Washington, D.C., pp. 337–346.

Langston, C.A., Hammer, K., 2001. The vertical component P-wave receiver function. Bull. Seismol. Soc. Am. 91, 1805–1819.

Li, X.-Q. (1996). Deconvolving orbital surface waves for the source duration of large earthquakes and modelling the receiver functions for the earth structure beneath a broadband seismometer array in the Cascadia subduction zone, Ph.D. Dissertation, 153 pp., Oregon State Univ., Corvallis, Sept. 1996.

Long, A.S., 2004. Postsurvey calibration of 3D seismic results to presurvey modeling predictions. Lead. Edge 23 (10), 1033–1036.

Meyers, E.V., Christensen, D., Abers, G., Pollock, M., 1999. Preliminary Results from BEAAR (Broadband Experiment across the Alaska Range). EOS Trans. AGU 80 (46), F711.

Morozov, I.B., 2004. Crustal scattering and some artefacts in receiver function images. Bull. Seismol. Soc. Am. 94 (4), 1492–1499.

Morozov, I.B., Dueker, K.G., 2003a. Signal-to-noise ratios of teleseismic receiver functions and effectiveness of stacking for their enhancement. J. Geophys. Res. 108. doi:10.1029/2001JB001692.

Morozov, I.B., Dueker, K.G., 2003b. Depth-domain processing of teleseismic receiver functions and generalized three-dimensional imaging. Bull. Seismol. Soc. Am. 93, 1984–1993.

Nabelek, J., Li, X.-Q., Azevedo, S., Braunmiller, J., Fabritius, A., Leimer, B., Tréhu, A.M., Zandt, G., 1993. A high-resolution image of the Cascadia subduction zone from teleseismic converted phases recorded by a broad-band seismic array. Eos, Trans. AGU 74 (43), 431 (Fall. Meet. Suppl.).

Nowack, R.L., Dasgupta, S., Schuster, G.T., Sheng, J., 2003. Correlation migration of scattered teleseismic body waves with application to the 1993 Cascadia experiment. EOS. Trans. AGU 84 (46), S32A–0835 (Fall Meet. Suppl).

Park, J., Levin, V., 2000. Receiver functions from multiple-taper spectral correlation estimates. Bull. Seismol. Soc. Am. 90 (6), 1507–1520.

Revenaugh, J., 2000. The relation of crustal scattering to seismicity in southern California. J. Geophys. Res. 105, 25,403–25,422.

Robertsson, J.O.A., Blanch, J.O., Symes, W.W., 1994. Viscoelastic finite-difference modelling. Geophysics 59 (9), 1444–1456.

Rondenay, S., Bostock, M.G., Shragge, J., 2001. Multiparameter two-dimensional inversion of scattered teleseismic body waves. 3. Application to the Cascadia 1993 data set. J. Geophys. Res. 106, 30795–30807.

Shearer, P.M., 1991. Constraints on upper mantle discontinuities from observations of long-period reflected and converted phases. J. Geophys. Res. 96, 18,147–18,182.

Sheehan, A.F., Shearer, P., Gilbert, H.J., Dueker, K.G., 2000. Seismic migration processing of P–SV converted phases for mantle discontinuity structure beneath the Snake River Plain, western United States. J. Geophys. Res. 105, 19,055–19,065.

Shen, Y., Solomon, S.C., Byarnason, I.T., Wolfe, C.J., 1998. Seismic evidence for a lower-mantle origin of the Iceland Plume. Nature 395, 62–65.

Trehu, A.M., Asudeh, I., Broher, T.M., Luetgert, J.H., Mooney, W.D., Nabelek, J.I., Nakamura, Y., 1994. Crustal architecture of the Cascadia Forearc. Science 266, 237–243.

Wagner, R.A., Langston, G.A., 1992. Body-to-surface wave scattered energy in teleseismic coda observed at the NORESS seismic array. Bull. Seismol. Soc. Am. 82, 2126–2138.